Plasma Sources Science and Technology

PAPER

Experimental observation and numerical investigation of imposed pattern formation in magnetized plasmas by a wide wire mesh

To cite this article: Mohamad Menati *et al* 2020 *Plasma Sources Sci. Technol.* **29** 085015

IOP Publishing Plasma Sources Science and Technology
Plasma Sources Sci. Technol. **29** (2020) 085015 (13pp) https://doi.org/10.1088/1361-6595/aba7ed

Experimental observation and numerical investigation of imposed pattern formation in magnetized plasmas by a wide wire mesh

Mohamad Menati[1,5], Taylor Hall[1], Behnam Rasoolian[2], Lénaïc Couëdel[3,4], Edward Thomas Jr[1] and Uwe Konopka[1]

[1] Department of Physics, Auburn University, Auburn, Alabama 36849, United States of America
[2] Department of Computer Science and Software Engineering, Auburn University, Auburn, Alabama 36849, United States of America
[3] Department of Physics and Engineering Physics, University of Saskatchewan, Saskatoon, SK S7N 5E2, Canada
[4] CNRS, Aix Marseille Univ., PIIM, UMR 7345, 13397 Marseille cedex 20, France

E-mail: mzm0085@auburn.edu

Received 2 May 2020, revised 1 July 2020
Accepted for publication 21 July 2020
Published 24 August 2020

Abstract

In this paper, the formation of imposed patterns due to placing a wide wire mesh ('waffle' electrode) in the bulk of a strongly magnetized ($B \geqslant 1$ T) plasma is investigated both experimentally and numerically. A new double head electrostatic probe was designed for the experiments that allows for measurements of the floating potential beneath the mesh in the magnetized plasma. The measurements using this probe revealed that due to the presence of the 'waffle' electrode in the bulk of the magnetized plasma, an organized pattern appears in the plasma potential. As a result of this imposed pattern, when dust particles were added to the experiments, they became trapped beneath the edges of the 'waffle' electrode. The effects of placing a wire mesh in the bulk of a magnetized plasma were further investigated using fluid and particle-in-cell (PIC) simulations. These simulations were able to qualitatively reproduce the experimental observations. The results of the simulations showed that the imposed patterns arise due to differences in the cross-field transport of the electrons and ions in the presence of magnetic field.

Keywords: magnetize plasma, magnetized dusty plasma, plasma filament, pattern formation in plasma, imposed structures in plasma

(Some figures may appear in colour only in the online journal)

1. Introduction

A complex (dusty) plasma, is a four component plasma which includes electrons, ions, neutral gas atoms, and charged microparticles. These plasmas have been a topic of interest in the study of astrophysical objects [1], such as interstellar clouds [2–4], planetary rings [5–7], comet tails [8, 9], and in the study of controlled plasma systems [10] such as fusion devices where hot ablated material from the walls can cause disruptions [11, 12]. Controlling the presence of these solid particles can be of technological importance in various low temperature plasma applications, such as plasma etching [13] or nanoparticle synthesis in plasma [14–16]. In many cases (for example the plasmas in fusion devices and astrophysical systems), the plasma is subjected to strong magnetic fields ($B \geqslant 1$ T). It is therefore crucial to study the physics of dust particles immersed in magnetized electric discharges [17, 18].

In a typical low temperature laboratory dusty plasma set-up, the dust particles have a charge to mass ratio of the order of $10^{-12} - 10^{-13} e/m_e$, where e is the elementary charge and

[5] Author to whom any correspondence should be addressed.

m_e the mass of an electron [19]. Because of this small charge-to-mass ratio, the charged dust particles require very high-magnetic fields to become magnetized [19, 20]. Therefore, the early dusty plasma experiments in the presence of magnetic field were focused on the rotation of the dust cloud caused by low to moderate magnetic fields ($B \leqslant 0.2$ T) [21–26]. It was observed in these studies that in this magnetic field regime, the 2-dimensional (2D) dust layers rotate as a rigid body due to ion drag force [21–26]. It was shown that the ion drag itself could be due to $E \times B$ drift or diamagnetic rotation of the ions [22, 23, 25]. The rotation of volumetric dust structures formed in magnetized glow discharges was recently studied by Dzlieva *et al* [27, 28] and Karasev *et al* [29]. In these works, the plasma was exposed to homogeneous [27, 28] and inhomogeneous magnetic fields [29]. High angular velocities of the order of 15 rad s^{-1} were reported for the dust cloud by Dzlieva *et al* [28].

By studying the dynamics of dust particles in magnetized plasmas, different parameters for dust particles such as charge, kinetic temperature, diffusion coefficient, and screening length may be also evaluated [30, 31]. At moderate magnetic fields ($B \leqslant 0.2$ T), Vasil'ev *et al* [30] determined the dynamical characteristics of dust particles by analyzing their displacement in a magnetized glow discharge. Recently, Melzer *et al* [31] studied the behavior of dust particles exposed to a wide range of magnetic field from few milliteslas to 5.8 T. They measured the dust particles properties at various magnetic field strengths and showed that they only slightly correlate with the strength of the applied magnetic field [31].

Several other phenomena may be observed in dusty plasma experiments exposed to strong magnetic fields ($B \geqslant 1$ T). Phenomena that can occur in the background plasma and/or the dust particles include but are not limited to shear flow instability [32–34], Kelvin–Helmholtz instability [35–37], dust particle charge fluctuation [38–40], dust voids [41–43], and of particular interest to this work, filamentation [44–48] and gridding phenomenon [49–51].

Plasma filaments can arbitrarily form in a low-pressure ($P \leqslant 30$ Pa) plasma that is exposed to a strong magnetic field. When viewed from the top, these filaments appear in different shapes, such as individual bright spots, spirals, and concentric rings that are extended through the plasma along the magnetic axis [44–48]. Moreover, Thomas *et al* [49] first observed that at magnetic fields $B \geqslant 1$ T, placing a metal wire mesh in the bulk of a dusty plasma generates imposed patterns in the plasma and dust cloud that reproduce the spatial structure of the wire mesh (gridding). This phenomenon was further experimentally studied in the MDPX device [49–51].

There are similarities between gridding phenomenon (dust pattern formation) and plasma filamentation that suggest they may arise from the same physical mechanism. Both phenomena highly depend on the magnetic field and neutral gas pressure, mostly appear in plasmas/dusty plasmas that are exposed to strong magnetic fields ($B \geqslant 1$ T), and they both are controlled by the ion dynamics [45, 51]. Also, these two phenomena can occur simultaneously in the plasma and if the dust particles number density is not too high, the presence of the dust particles does not significantly affect the filamentation [52].

The study of these phenomena is relatively new and there have been only a few theoretical or numerical investigations on gridding [53] and filamentation [48, 54]. In this paper, we present a combination of experimental and numerical studies on both phenomena which indicate that the gridding of dust particles arises from imposed filaments originating at the mesh. This work is mostly focused on the study of the background magnetized plasma in the presence of the metal mesh to find an explanation for the gridding of the dust particles. It will be shown that the effect of the strong magnetic field on the cross-field transport of the electrons and ions results in a difference between their densities within the imposed filaments. This density imbalance between electrons and ions leads to the emergence of a potential structure in the plasma parallel to the magnetic axis that reproduces the spatial structure of the grid. This potential structure is strong enough to trap the dust particles and cause gridding phenomenon.

This article is organized as follows. Section 2 presents recent experimental observations of the induced gridding phenomenon when a wide metal mesh is inserted in a highly magnetized low temperature plasma. Fluid and particle-in-cell simulations results are discussed in section 3. Finally, section 4 provides a summary and conclusion of the work.

2. Experimental observations

The specific experiments described here were conducted in the MDPX vacuum vessel using a large grid-like, or 'waffle' shaped, electrode to create imposed, ordered structures. The design and capabilities of the MDPX device have been extensively described previously and so the description of the experiments here will only include the main details relevant to this work [19, 55]. For the experiments presented here, argon plasma was generated using capacitively coupled radio-frequency (RF) electrodes. The bottom electrode was powered with 5 W of RF power at 13.56 MHz, and the top electrode was electrically floating. The neutral gas pressure was between (3.3–10 Pa) and the magnetic field ranged from 0–3 T. Measurements with a double Langmuir probe resulted in measurements of the electron temperature in the range of $T_e =$ 3–3.5 eV, and electron densities of $n_e = 0.2$–1×10^9 cm^{-3}. The resulting electron Debye lengths range from $\lambda_{De} =$ 0.4–1.0 mm.

The previously mentioned 'waffle' electrode was designed to allow spatially resolved measurements beneath the grid with a spatial resolution better than the characteristic length of the grid. In previous experiments, the wires used to build the conducting mesh were small (200–300 μm). Consequently the used plasma probes were larger (1–2 mm) than the wire dimensions and did not have the accuracy to resolve plasma parameters beneath the individual wires of the mesh. The 'waffle' electrode (see figure 1(a)) is a 0.64 cm thick aluminum square of 7.2 cm on each side with six 1.6 $\times$ 1.8 cm rectangular holes giving the electrode its 'waffle' design. The electrode was attached to an aluminum rod within a ceramic tube. An 's'-shaped arm allowed us to position the electrode 8.25 cm

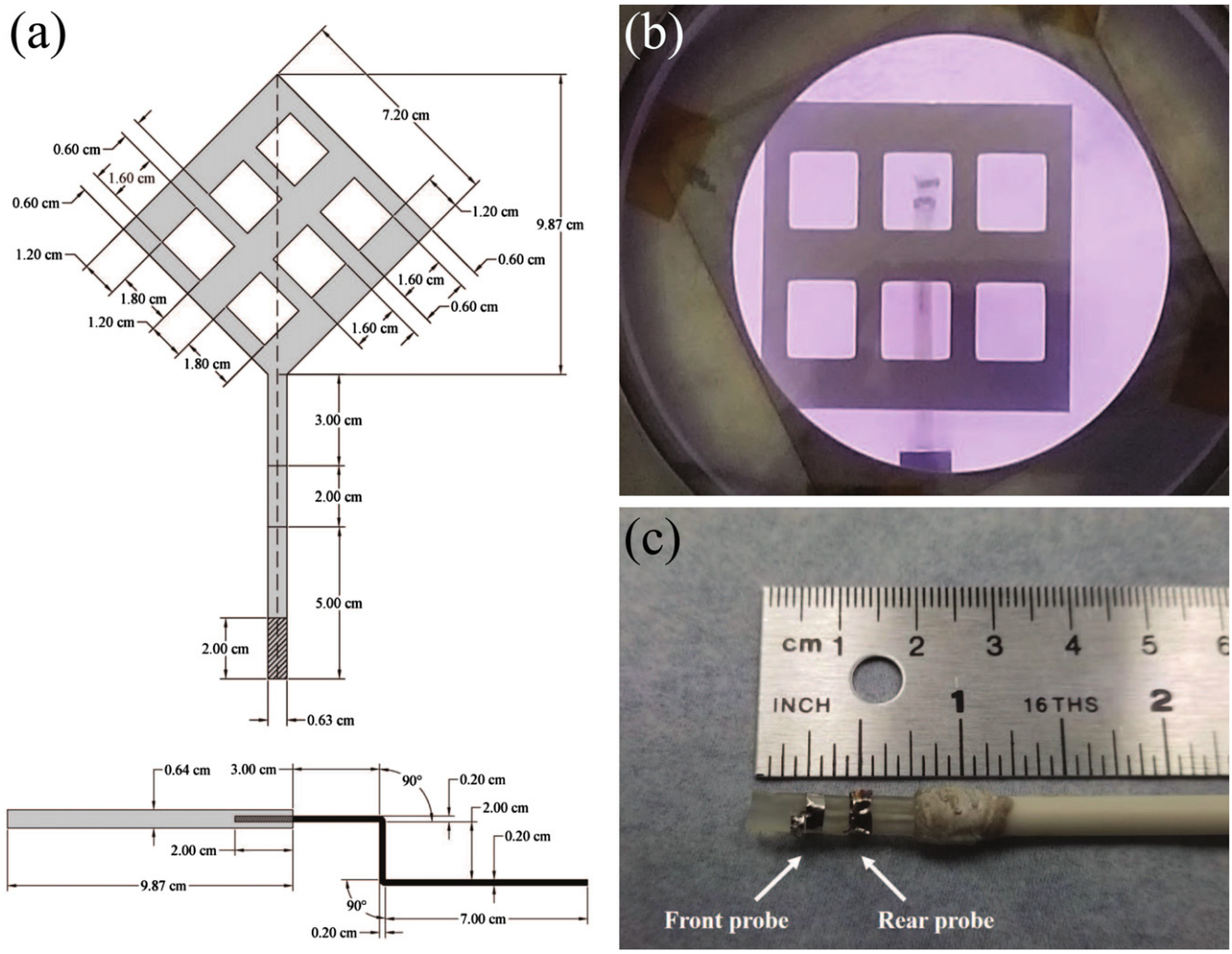

Figure 1. (a) Top and side schematics of grid-like 'waffle' electrode. (b) Top down view of the 'waffle' electrode in the vacuum chamber where the ring probe can be seen beneath the electrode. (c) Ring probes and 3D printed probe head. The probe head is made of a photocured polyacrylate, 25.4 mm in length with a 4.76 mm diameter. The probe tips are stainless steel sheet metal 4.76 mm wide and have a center-to-center spacing of 5.55 mm.

above the bottom electrode at the center of the vacuum vessel. A direct-current (dc) bias, $V_g = \pm 40$ V could be applied to the 'waffle' electrode.

Also, a new electrostatic probe, the ring probe (RP), was designed for these experiments. It can be seen beneath the 'waffle' electrode in figure 1(b) and to scale in figure 1(c). The intent of this probe design is to allow for measurements of the floating potential (and subsequently, the electric field) within the plasma even at high magnetic fields when the ion and electron flows become strongly constrained by the magnetic field. This is accomplished by using two stainless steel rings, 2.4 mm wide and 4.76 mm in diameter, wrapped around a 3D printed probe head, made of photocurable polyacrylate. The gap between the rings is 3.18 mm and the center to center spacing, Δx, is 5.55 mm. Each of the probe heads were electrically floating within the plasma. To replicate the conditions under which dust particles could be confined, a CF Flange copper gasket (8.23 cm outer diameter and 6.38 cm inner diameter) was placed on the lower electrode and centered beneath the 'waffle' electrode. When dust particles are present, this ring allows for a small radial electric field which confines the dust particles. Note that no dust particles were present in the plasma while performing measurements with the ring probe. Figure 2 displays the overall scheme of the set up with the discharge electrodes, 'waffle' electrode, and the ring probe in the MDPX vacuum chamber.

The floating potential measurements were made at a sampling rate of 50 kHz and 5000 samples were collected for each measurement. The ring probe was inserted into the plasma 2.9 cm below the 'waffle' electrode and its horizontal position X_{RP} was incrementally stepped horizontally ($\delta x = 0.1$ cm) through the vacuum chamber taking measurements at each position ($X_{RP} = 0.0$ cm corresponds to the center of the vacuum vessel). The floating potential signals are first processed by averaging the measured signal at each position X_{RP}. This process is then repeated at each unique position X_{RP} giving a profile of the floating potential as a function of X_{RP} for each RP tip. The floating potential profiles are then smoothed by computing a moving average. Examples of profiles are shown in figure 3 for the experimental conditions of $B = 0$–3.07 T, $P = 3.3$ Pa, and $V = +40$ V bias on the 'waffle' electrode. Although, we choose to only display the

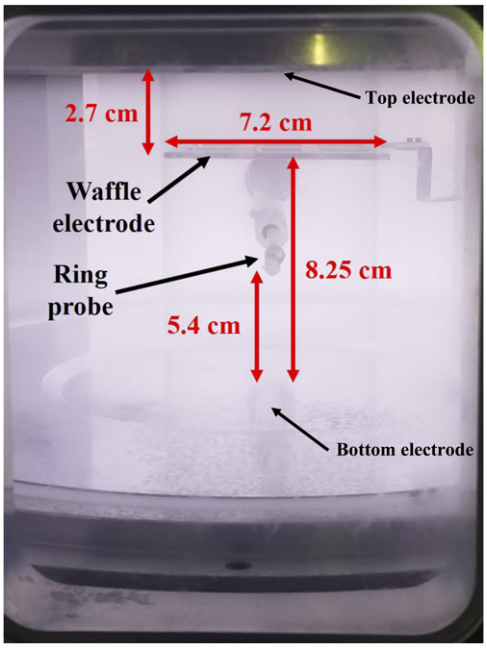

Figure 2. Overall scheme of the set up with the discharge electrodes, 'waffle' electrode and the ring probe in the MDPX vacuum chamber.

results for $P = 3.3$ Pa, there is not any significant difference in the results obtained in the mentioned range of pressures (3.3–10 Pa).

The horizontal electric field at the middle-point between the two ring probes was calculated according to the formula:

$$E_x = \frac{-(V_{f_1} - V_{f_2})}{\Delta x}, \quad (1)$$

where V_{f_1} is the floating potential measured by the front ring, V_{f_2} is the floating potential measured by the rear ring. Calculated electric fields are shown in figure 4 as solid black lines, with error bars of $\pm 1\sigma$ where σ is the standard deviation. The electric field determined from the ring probe measurements is a combination of a confining electric field from the confining ring, and a contribution from the 'waffle' electrode. The electric field component from the confining ring is shown in red in figure 4, with the effective electric field component from the 'waffle' electrode shown in blue. This confining electric field is determined from a cubic fit of the ring probe measurements. This fit was chosen for its odd parity, to maintain opposing electric field directions at distances far from the center, and so as not to over-fit the data with a higher order polynomial. The effective electric field has been calculated by subtracting the confining electric field (background electric field) from the total electric field calculated from the probe measurement. The total electric field is shown as solid black lines in figure 4.

The effective electric field due to the presence of the 'waffle' electrode is plotted in figure 5 as two-dimensional contour plots. These contour plots display the effective electric field as a function of magnetic field strength on the horizontal axis, and the position X_{RP} (with respect to the center of the chamber) on the vertical axis (see figure 5). Areas of red represent positive electric fields, and areas of blue represent negative

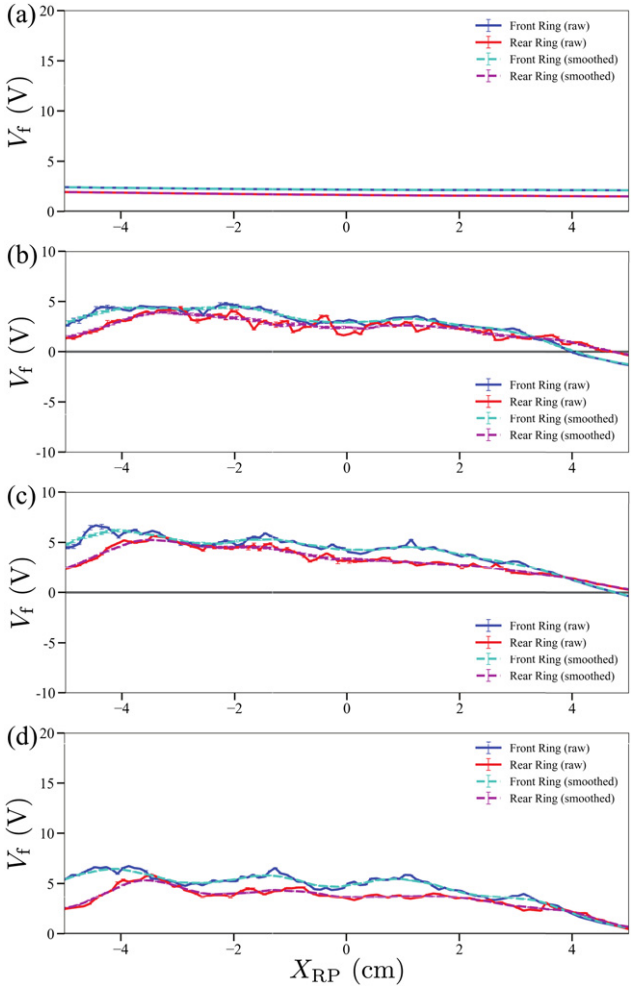

Figure 3. Floating potential profiles for a range of discharge parameters: (a) $B = 0.0$ T, $P = 3.4$ Pa, $V_g = +40$ V; (b) $B = 1.02$ T, $P = 3.4$ Pa, $V_g = +40$ V; (c) $B = 2.05$ T, $P = 3.4$ Pa, $V_g = +40$ V; (d) $B = 3.08$ T, $P = 3.3$ Pa, $V_g = +40$ V. The floating potential profile for the RP front ring is shown in blue, with its smoothed profile shown in cyan. The floating potential measurements for the RP rear ring are shown in red, with its smoothed profile shown in magenta. $X_{RP} = 0.0$ cm corresponds to the center of the vacuum vessel.

electric fields. White areas indicate the regions where the electric field has no net $x-$component due to the presence of the 'waffle' electrode. These are thus regions where no net horizontal electric force would act on charged micro-particles. The grey horizontal bands overlaid on the contour plots represent the position of filled region of the 'waffle' electrode.

The contour plot of the electric field as a function of magnetic field strength and the position of the probe (figure 5) allows us to identify the appearance of structure in the electric field. At low magnetic field, $B \leqslant 0.5$ T, no structure within the electric field can be clearly defined. It therefore does not provide evidence of an imposed ordered structure phenomenon. For a bias of $V = +40$ V on the 'waffle' electrode a structuring of the electric field is observed for $B \geqslant 1.0$ T, and for a bias of $V = -40$ V a similar structure is observed for $B \geqslant 1.5$ T. This effect can be seen more clearly between 0.6 and 2.4 cm in both plots and between -2.4 and -0.6 cm for the $V = +40$ V plot

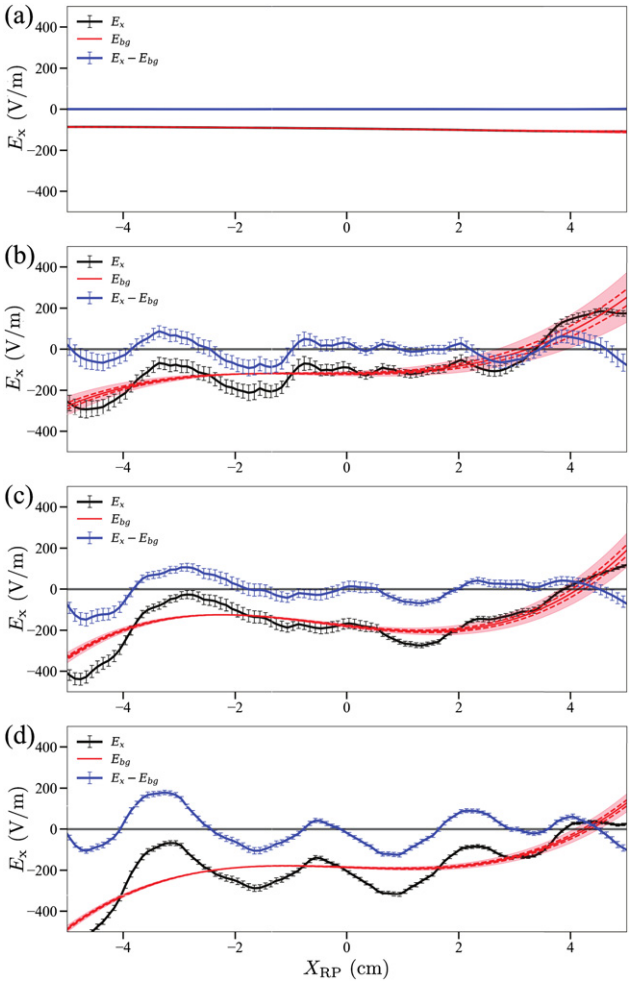

Figure 4. Calculated x–components of the electric fields E_x for different discharge parameters: (a) $B = 0.0$ T, $P = 3.4$ Pa, $V_g = +40$ V; (b) $B = 1.02$ T, $P = 3.4$ Pa, $V_g = +40$ V; (c) $B = 2.05$ T, $P = 3.4$ Pa, $V_g = +40$ V; (d) $B = 3.08$ T, $P = 3.4$ Pa, $V_g = +40$ V. Electric fields, E_x, derived from the floating potential measurements are shown as the solid black lines. Background electric fields from the confining ring, E_{bg}, are shown as a solid red line, with the $\pm 1\sigma$ confidence interval given as red dashed lines, and the $\pm 3\sigma$ confidence interval given as the red shaded area. The electric field x–component due to the 'waffle' electrode, the difference between the total field and the background, $E_x - E_{bg}$, is shown as the solid blue line. $X_{RP} = 0.0$ cm corresponds to the center of the vacuum vessel.

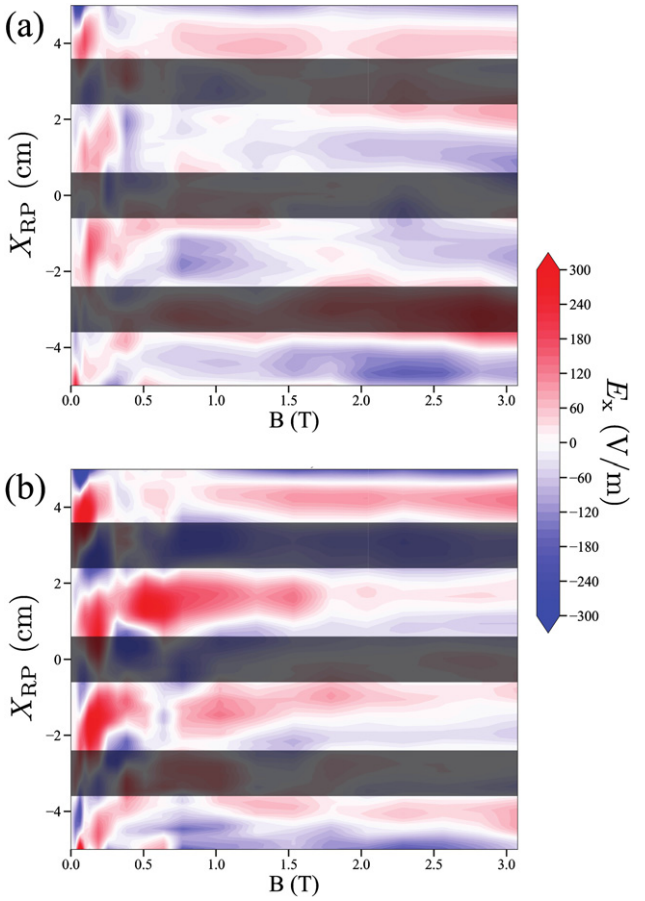

Figure 5. Contour plots of effective electric field as a function of chamber position and magnetic field for a neutral pressure of $P = 3.4$ Pa and 'waffle' electrode bias of: (a) $V_g = -40$ V and, (b) $V_g = +40$ V. The dark gray bars overlaid on the contour plots show the location of the conducting bands of the electrode. Plots are colored red for regions of positive ($+x$–direction, up) electric field and blue for negative ($-x$–direction, down) electric field.

on the bottom. For a negatively charged dust particle, which is typical for the laboratory dusty plasmas studied in the MDPX, the forces on the dust particles would be in opposite direction of the electric field. These measurements then indicate that it is the regions beneath the holes and near the edges of the 'waffle' electrode (regions in white with red color at the top and blue at the bottom), which are the most probable locations for the dust particles to be trapped. It has to be noted that the ion drag force which will be in opposite direction of the electric force might affect the locations where the dust particles get trapped in the presence of the mesh. Figure 6 shows the location of the dust particles in plasma beneath the 'waffle' electrode for two magnetic field strengths ($B = 0$ T and $B = 1.02$ T). This figure illustrates the experimental observation of dust particle trapping beneath the edges of the 'waffle' electrode.

3. Numerical simulations

3.1. Fluid simulations

3.1.1. Model overview. In order to investigate the cause of the gridding phenomenon, a 3-dimensional (3D) fluid model has been developed to study the effect of placing a metal mesh on the plasma. No dust particle has been considered in any of the numerical simulations presented in the current work. Although our numerical model is strongly inspired by the aforementioned experiments, it is not an exact replication of the experimental set-up. The experimental geometry is simplified allowing simulation to be run with reasonable CPU time. A full description of the numerical model has recently been published [54]. Therefore, only a brief summary of its key features is given below.

In our 3D fluid model, both electrons and ions are taken into account. The full set of equations of the model is given below:

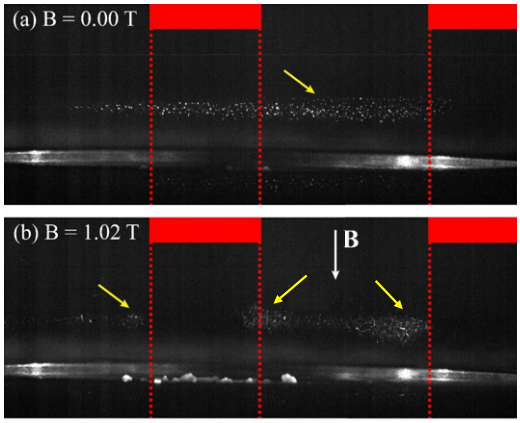

Figure 6. The position of dust particles beneath the 'waffle' electrode with and without applied magnetic field for a neutral pressure of $P = 3.4$ Pa and 'waffle' electrode bias of $+40$ V. The positions of the wires of the 'waffle' electrode are indicated using red rectangles. The yellow arrows point to the dust particles. At $B = 0$ the dust particles are randomly distributed beneath the 'waffle' electrode and do not get affected by it while at $B = 1.02$ T, the dust particles are mostly trapped beneath the edges of the 'waffle' electrode.

$$\nabla^2\varphi = -\frac{\rho}{\epsilon}, \tag{2}$$

$$q_\alpha n_\alpha (\mathbf{E} + \mathbf{V}_\alpha \times \mathbf{B}) - \nabla \mathbf{P} - m_\alpha n_\alpha \nu_{\alpha n} \mathbf{V}_\alpha = m_\alpha \frac{\mathrm{d}\mathbf{V}_\alpha}{\mathrm{d}t}, \tag{3}$$

$$\Gamma_\alpha = n_\alpha \mathbf{V}_\alpha, \tag{4}$$

$$\frac{\partial n_\alpha}{\partial t} + \nabla \cdot \mathbf{\Gamma}_\alpha = \sigma_\mathrm{I} - \sigma_\mathrm{L}, \tag{5}$$

where the α subscript represents the electrons (e) or the ions (i), φ is electric potential, ρ charge density, ϵ electric permittivity, q_α electric charge, n_α density, $\mathbf{E} = -\nabla\varphi$ electric field vector, and $\mathbf{B}$ is magnetic field vector. Also, P is neutral gas pressure, m_α is mass, $\nu_{\alpha n}$ collision frequency with neutral atoms, $\mathbf{V}_\alpha$ velocity vector, $\mathbf{\Gamma}_\alpha$ flux vector, σ_I ionization rate, and σ_L is recombination rate of the electrons and ions.

The four equations above are: the Poisson's equation for determining the electric potential from the plasma densities (equation (2)), the momentum equation to calculate the fluxes of the electrons/ions (equation (3)), the electrons/ions fluxes as a function of their densities and respective velocity vectors (equation (4)), and the continuity equation to update the local electron/ion densities according to their corresponding fluxes and ionization/recombination terms (equation (5)).

In our model, the temperatures of both electrons and ions are constant and therefore, energy equation is not included in the model [56–58]. Moreover, electron and ion losses only occur at the walls (plasma chamber or the metal mesh) and ionization is only considered to compensate for the loss of particles. The ionization rate is assumed to be proportional to the local electron density in the plasma. This formulation has been successfully used by other authors [59–64].

The computational space in this model includes a 6.3 cm $\times$ 6.3 cm $\times$ 4.2 cm ($X \times Y \times Z$) rectangular plasma chamber with grounded metallic walls. The metal mesh is also grounded

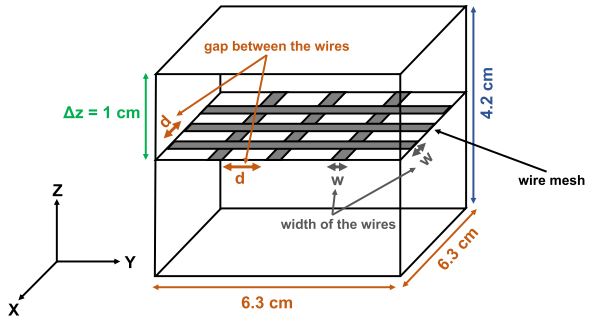

Figure 7. Schematic picture of the rectangular plasma chamber with a metal mesh placed at $\Delta z = 1.2$ cm below the top electrode. 'w' indicates the width of the wires and 'd' indicates the gap between the wires of the mesh. The dimensions of the chamber are displayed on the picture. The picture is not drawn to scale.

and placed at a distance $\Delta z = 1.2$ cm below the top electrode. The gridding phenomenon is studied using three different metal meshes with wires of width $w = 1.4$, 2.8 and 5.2 mm. A schematic picture of the simulated rectangular plasma chamber with a metal mesh placed below the top electrode is shown in figure 7.

Note that although in the experiments a bias voltage was applied to the metal mesh, the nature of the gridding phenomenon does not strongly depend on the bias voltage. Indeed, despite some slight differences, the experimental results with an unbiased grounded mesh are comparable to the results obtained with biased mesh [65]. Also, since the energy equation is not included in our model, applying a bias voltage to the mesh would cause unnecessary numerical difficulties.

Electron/ion densities are assumed to be uniformly fixed at 5×10^8 cm^{-3} at the beginning of each simulation. The constant electron and ion temperatures are set to be $T_\mathrm{e} = 2.5$ eV and $T_\mathrm{i} = 0.025$ eV, respectively. The background gas is argon that is exposed to $B = 1$ T magnetic field in negative z-direction. The numerical results were obtained in pressure range of $P = 4$–12 Pa. Since the simulation results at low and high neutral pressures were similar, we choose to display the results only for $P = 12$ Pa. This is because the plots at this pressure look neater as the higher collisionality of the plasma washes out the local disorganizations more effectively.

Based on the plasma parameters considered in the fluid model, Debye length, gyro-radius, mean-free-path for collision with neutral atoms, and Hall parameter for electrons and ions are presented in table 1. Hall parameter is the indicator of magnetization for any charged species in the plasma and is defined as the fraction of its mean-free-path to its gyro-radius. It is noted that for the assumed range of plasma parameters, electrons are strongly magnetized having a Hall parameter of 483.9, while ions are only moderately magnetized with a Hall parameter of 4.75.

Furthermore, different simulations have shown that the filamentary patterns due to the presence of the metal mesh appear in the magnetized plasma at time scales of $\sim$ 20–30 μs as also reported previously by Menati *et al* [48]. Consequently, the numerical data from the fluid simulations presented in this

Table 1. Debye length, gyro-radius, mean-free-path for collision with neutral atoms, and Hall parameter (as the indicator of magnetiaztion) for electrons and ions in the fluid simulations. These parameter are calculated for Argon plasma having number density of 5×10^8 cm^{-3}, exposed to $B = 1.0$ T magnetic field. Electron and ion temperatures are considered to be $T_e = 2.5$ eV and $T_i = 0.025$ eV, respectively, and neutral gas pressure is assumed to be $P = 12$ Pa.

Species	Debye length (m)	Gyro-radius (m)	Mean-free-path (m)	Hall parameter
Electron	5.10×10^{-4}	6.20×10^{-6}	3.0×10^{-3}	483.9
Ion	5.10×10^{-5}	1.60×10^{-4}	7.60×10^{-4}	4.75

work represent evolution of the plasma over a time span of 25 μs.

3.1.2. Fluid simulation results. In the first numerical simulation of the gridding phenomenon, a metal mesh with wires of width $w = 1.4$ mm is placed at $\Delta z = 1$ cm below the top electrode. The gap between the wires of the mesh is $d = 8$ mm. The top-view and side-view of the electron density profile due to the presence of this wire mesh is shown in figure 8. The side-view of the electron density profile is presented only for the region beneath the mesh. The shape of the ion density profile is the same as that of the electron, and is therefore not shown here. It can be seen from figure 8 that the presence of the metal mesh has induced filamentation in the plasma that is extended parallel to the magnetic field.

In the presence of the strong magnetic field, the diffusion of the electrons and ions perpendicular to the magnetic field is reduced. They mostly diffuse parallel to the magnetic field to the metal mesh and the walls of the plasma chamber. Since they reach the metal mesh before the top electrode, depletion regions form right below the wires of the mesh which we call primary depletion regions. Additional depletion regions appear half way between the primary depletion regions, which will be called secondary depletion regions (see figure 8). In the simulations where the gap between the mesh wires was less than $d = 3$ mm, the secondary depletion regions did not appear in the plasma. Because of the very fine structure of the narrow meshes, the formation of the secondary depletion regions could not be experimentally investigated.

The density of the electrons and ions in the depletion regions differ from each other as displayed in figure 9(a). Also, in the neighboring regions on the sides of the depletion regions, the electron/ion densities are higher than the initial plasma density which was set to be 5×10^8 cm^{-3}. Because of the much smaller mass of the electrons, they diffuse much faster than the ions to the metal mesh parallel to the magnetic axis, leaving the heavy ions behind. Although the cross-field diffusion of both electrons and ions is suppressed by the magnetic field, the larger mass of the ions enables them to have a limited diffusion across the magnetic field [66]. Therefore, while still diffusing mostly parallel to the magnetic field, the ions beneath the mesh wires can partially diffuse to the gap between the wires. This cross-field diffusion is due to the repulsive force caused by the excess of the ions in those regions. If the excess of the ions is not relieved, it would decrease the diffusion of the electrons parallel to the magnetic field and interrupt the formation of the depletion regions beneath the wires. This continuous process results in a depletion region beneath the mesh

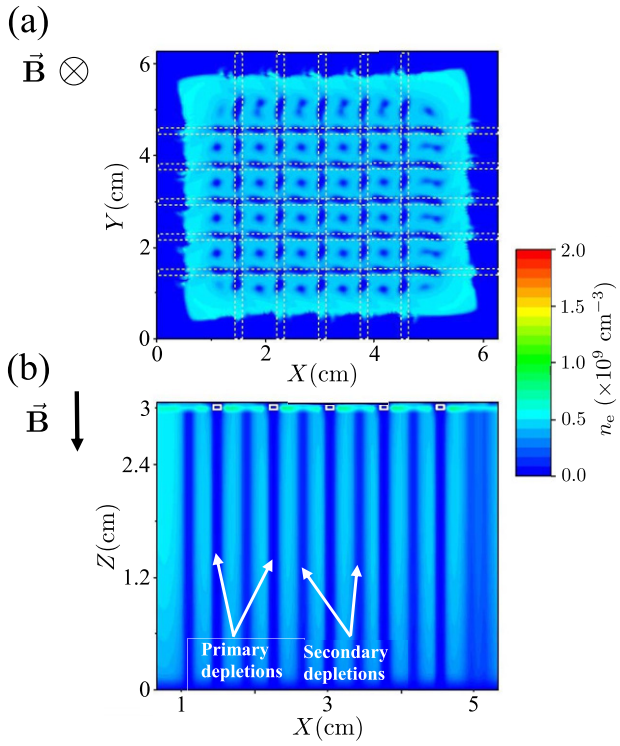

Figure 8. (a) $X - Y$ and, (b) $X - Z$ cross sections of the electron density profile of an argon plasma at a pressure of 12 Pa exposed to $B = 1$ T magnetic field. A metal mesh with wires of width $w = 1.4$ mm is placed $\Delta z = 1$ cm below the top electrode. The $X - Y$ profile is taken at $Z = 1.5$ cm from the bottom electrode and The $X - Z$ profile is taken at $Y = 3$ cm. The $X - Z$ cross section is only displayed from the bottom electrode to the mesh in Z direction and away from the sheath regions in X direction. The position of the metal mesh is indicated on the graphs using white lines.

and regions with enhanced electron/ion densities in the gap between the wires.

This process may also explain the appearance of the secondary depletion regions (see figure 8). The repelled ions from beneath the wires sit in the gaps where the repulsive force from the excess of the ions and gradient of density are at equilibrium and create a region with enhanced plasma density. If the gap between the mesh wires is big enough ($d \geqslant 3$ mm for the assumed plasma parameters in these simulations), these repelled ions can also repel their neighboring ions and create secondary depletion regions.

The outcome of the density imbalance in figure 9(a) is the plasma potential profile that is displayed in figure 9(b). This potential profile which is extended along the magnetic

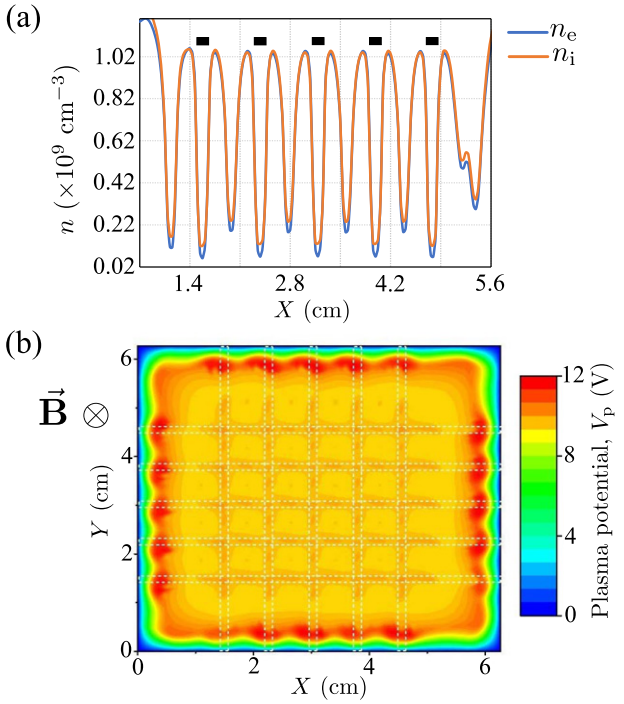

Figure 9. (a) Electron and ion densities along X-axis at $Y = 3$ cm and $Z = 1.5$ cm which shows a difference in electron and ion densities especially in the depletion regions (due to the presence of a metal mesh with wires of width $w = 1.4$ mm). The position of the mesh wires are indicated using small black boxes. (b) The plasma potential profile in $X - Y$ plane as a result of this density difference. The plasma parameters are the same as figure 8, $P = 12$ Pa and $B = 1$ T. This potential profile is extended along the magnetic field in Z direction. The position of the metal mesh is indicated using white dashed lines.

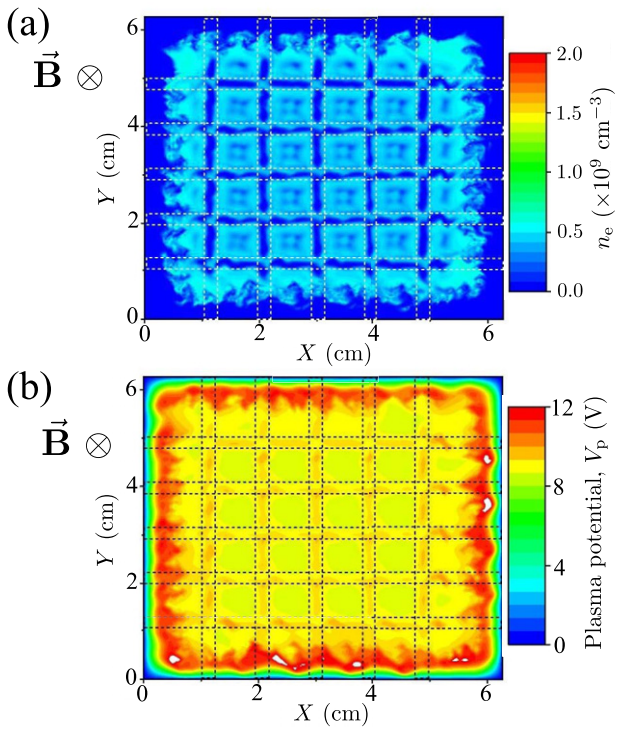

Figure 10. $X - Y$ cross sections of (a) the electron density profile and (b) plasma potential of an argon plasma at pressure of 12 Pa exposed to $B = 1$ T magnetic field. A metal mesh with wires of width $w = 2.5$ mm is placed 1 cm below the top electrode. The profiles are taken at $Z = 1.5$ cm. The position of the metal mesh is indicated using dashed lines.

field is responsible for trapping the negatively charged dust particles and generating the gridding phenomenon. Although, we are not exactly simulating the experimental set up, the results and the magnitude of the plasma potential are similar to the observations reported in previous experiments performed using narrow meshes with wire of width $w \leqslant 1$ mm [49, 51].

In order to further investigate the gridding phenomenon, the simulations were repeated using two other meshes with wire width $w = 2.8$ mm and $w = 5.2$ mm. The gap between the mesh wires was again set to $d = 8$ mm. The electron density profile and the plasma potential for these two cases are presented in figures 10 and 11, respectively. Through these figures, the transition from one depletion region to two depletion regions (in the density and potential profiles) beneath the mesh wires by increasing the wire width w can be clearly seen. These two depletion regions tend to form at the edges of the wires while the single depletion region that forms in the presence of narrow meshes appears right below the wires of the mesh (see figure 8).

The difference in the location of the depletion regions also shifts the regions with higher plasma potential to the edges of the mesh wires as it is illustrated in figure 12. In this figure, the $X - Z$ cross-section of plasma potential profiles caused by the meshes with wires of width $w = 1.4$ mm and $w = 5.2$ mm are plotted. It is clear that in the presence of the wide mesh ($w = 5.2$ mm), the regions at higher plasma potential form beneath the edges of the wires, while for the narrow mesh ($w = 1.4$ mm), there is only one region at higher potential right below its wires. These results may explain the observations presented in figures 5 and 6 that in a gridding experiment with a wide mesh, the dust particles tend to be trapped beneath the edges of the 'waffle' electrode.

Based on the description that was proposed for the formation of secondary depletion regions, an explanation can be also given for the appearance of the potential pattern and trapping of dust particles beneath the edges of the 'waffle' electrode (figures 5 and 6). When the mesh wires are wide ($w = 5.2$ mm), only the regions beneath the edges of the wires can interact with the regions beneath the gaps. Therefore, the excess of the ions beneath the center of the wires cannot be revealed and as stated before, this will interrupt the formation of depletion regions. Consequently, depletion regions with higher electrostatic potential can only form in the transition region beneath the edges of the wide wire mesh ('waffle' electrode). It has to be noted that the exact location of the trapped dust particles in such a potential structure is defined not only by the electrostatic force from the electric field but also by neutral and ion drag forces. Currently, it is not computationally possible to add dust particles to the fluid model to precisely study their behavior in the observed potential structure.

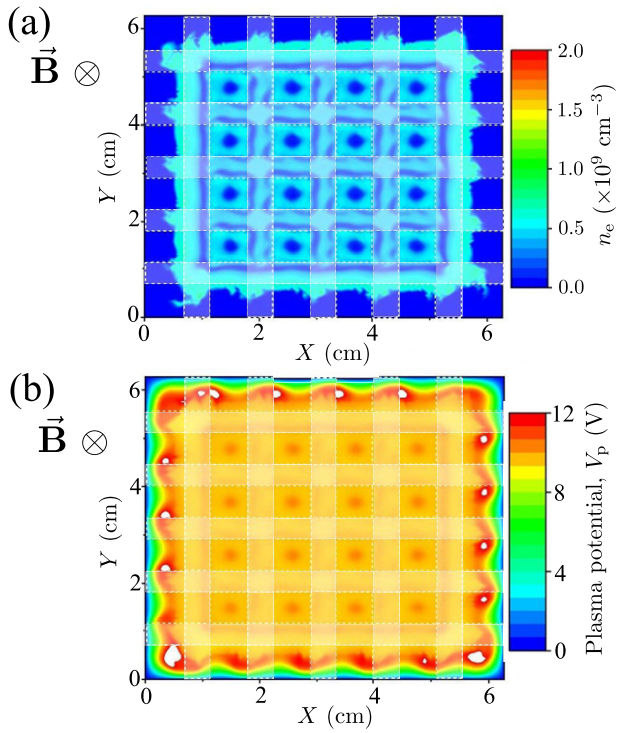

Figure 11. $X - Y$ cross sections of (a) the electron density profile and (b) plasma potential of an argon plasma at pressure of 12 Pa exposed to $B = 1$ T magnetic field. A metal mesh with wires of width $w = 5.2$ mm is placed 1 cm below the top electrode. The profiles are taken at $Z = 1.5$ cm. The position of the metal mesh is indicated using transparent masks and white dashed lines.

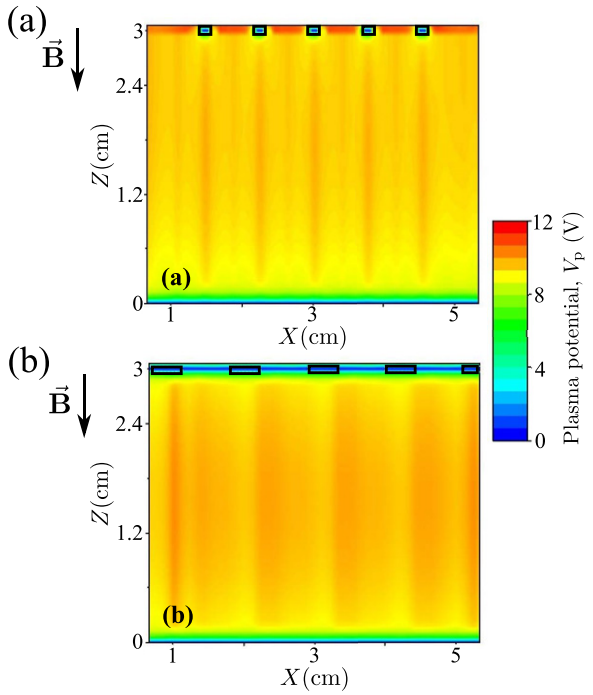

Figure 12. $X - Z$ cross sections of the plasma potential profile of an argon plasma at pressure of 12 Pa exposed to $B = 1$ T magnetic field. (a) A metal mesh with wires of width $w = 1$ mm is placed 1 cm below the top electrode. (b) A metal mesh with wires of width $w = 5.2$ mm is placed 1 cm below the top electrode. The $X - Z$ profile is taken at $Y = 3$ cm and is only displayed from the bottom electrode to the mesh in Z-direction and away from the sheath regions in X-direction. It is obvious from these figure that the locations of the higher plasma potential to trap the dust particles are shifted to the edge of the mesh wires in the case of $w = 5$ mm mesh. The position of the metal meshes are indicated using small black rectangles.

3.2. *Particle-in-cell simulations*

3.2.1. Simulation parameters. Complementary two-dimensional (2D) PIC simulations of the RF argon discharge have been also performed. The aim of these simulations was to explore in greater details the influence of the boundary conditions such as the bias V_g of the grid and to take into account the secondary electron emission due to ion impact on the electrode and the grid [67, 68]. For this purpose, a simplified model of our discharge chamber was used and the simulations were run using the VSIM software from TechX corporation [69]. The simulation box had a width of 75 mm. Periodic boundary condition were used in the X-direction. The upper electrode was grounded and the powered electrode was located at the bottom at a distance of 27.5 mm from the upper electrode. The wire grid was simulated by considering three rectangular wires of width $w = 3$ mm and height $h = 0.5$ mm separated by a distance $d = 4.5$ mm, placed at the center of the chamber. The wires were positioned 20.6 mm above the powered electrode and were either grounded or biased at voltage $V_g = \pm 60$ V. All surfaces were considered to be perfect absorbers with a secondary electron emission probability due to ion impact of 10%. This value is close to the one reported in the literature for low energy ions impacting metal surfaces [70].

For every PIC simulation presented in this article, the powered electrode was connected to a 13.56 MHz RF voltage source with a constant peak-to-peak amplitude $V_{pp} =$ 108 V. In addition, a constant vertical magnetic field up to 0.5 T could be imposed. A constant background argon pressure $P = 13.25$ Pa was maintained between the electrodes. Only electron impact ionization, electron-impact excitation and electron elastic collision were considered in our simulations. Ion collisions with the neutral background were ignored thus reducing the ion diffusion perpendicular to the magnetic field lines. The pressure value was high enough to maintain a stable plasma in the studied range of parameters. Since the simulations were performed at a constant peak-to-peak RF voltage instead of constant RF power (as in the experiment), the simulated plasma density could not be directly compared to the experimental ones. Moreover, the external circuit was not simulated and no additional dc self-bias was therefore present on the powered electrode. Consequently, PIC simulation results only give qualitative information of the behavior of the discharge under different magnetic field strengths and grid bias voltages. The main advantages of the PIC simulations over our fluid simulation was the capacity to simulate RF excitation and heating of the electrons as well as taking into account the influence of secondary electron emission. However, contrary to the fluid model, the 2D geometry of the PIC simulations does not allow for a proper detailed investigation of the influence of the geometry of the grid.

3.2.2. PIC simulation results. A simulation without magnetic field and without bias on the grid was first run in order to obtain the undisturbed plasma parameters profile. The simulation was started with uniform ion and electron densities all over the simulation space ($n_0 = 10^9$ cm^{-3}) with electron and ion temperatures of $T_e = 3$ eV and $T_i = 0.027$ eV, respectively. The simulation was then run for 250 RF cycles. This was enough to reach steady state. The results are presented in figure 13(a). Each presented profile is averaged over 5 RF period in order to eliminate most of the fast fluctuations. It can be seen, apart from the sheath regions close to the electrodes and around the wires, the ion and electron densities are uniform and the plasma potential V_p is constant. Therefore the electric field is null in the bulk plasma and has no $x-$component in the sheath above the powered electrode. The plasma parameters profiles obtained at $B = 0$ T and $V_g = 0$ V are the reference profiles and served as input profile for for every other simulation.

The second simulation was run for $B = 0$ T and $V_g = -60$ V. As it can be seen in figure 13(b), the effect of the grid bias are not very important. Only a small increase of the electron and ion densities can be seen, especially just beneath the grid. This is due to the larger electric fields due to the bias of the grid. This effect might not be observable experimentally since the external circuit is not simulated and experiments are performed at constant RF power instead of constant RF amplitude. In addition, the sheath around the wires are slightly wider. The plasma potential in the bulk of the plasma is not displaying any significant influence from the presence of the biased wires. The electric field is therefore quasi-null in the bulk plasma, and no $x-$component of the electric field can be measured in the sheath above the powered electrode beneath the wires. These results are expected since the electrons and ions are able to diffuse in every direction and can shield the wires at distances over a few Debye lengths.

The third simulation was run for $B = 0.5$ T and $V_g = 0$ V. It can be seen in figure 13(c) that the magnetic field has a very noticeable effect on the plasma parameters. Just beneath the wires, the ion and electron densities are enhanced with respect to the regions of the discharge far from the wires. Moreover, just below the edges of the rectangular wires, the ion and electron densities are even higher on a narrow band that extends vertically down to the sheath above the powered electrode (see figure 13(c)). In the gap between the wires, it seems that there are depleted plasma regions that resemble the one observed in the fluid simulation. The effect on the plasma potential is not as important but nevertheless visible. Clear vertical structures in the plasma potential profile appear in the plasma even though the magnetic field is not as strong as in the experiments or in the fluid simulations. The plasma potential structures being quite weak, the structures on the $x-$component of the electric field are weak. This simulation nevertheless confirms the results obtained with the fluid simulations and shows the importance of the reduced diffusion of the charged species across the magnetic field lines.

The fourth simulation was run for $B = 0.5$ T and $V_g = -60$ V. As it can be seen in figure 13(d), the magnetic field has a strong effect on every plasma parameter. The ion and electron densities are strongly enhanced just beneath the wires, while between the wires, the plasma density is reduced. Far away from the wires, the plasma density is also increased with respect to the reference case at $B = 0$ T and $V_g = 0$ V and the case at $B = 0.5$ T and $V_g = 0$ V. The plasma potential profile is now strongly influenced by the presence of the biased mesh and the structures propagate vertically down to the sheath above the powered electrode. Note that the plasma potential beneath the wire is lower than in between the wire and far away from the grid. The potential structure is passed on the $x-$component of the electric field and its large $x-$component can be seen just beneath the edge of the wires. Since the electrons are confined along the magnetic field lines, the electrons beneath the wires are pushed away by the strong negative bias and remain confined in these regions. Moreover, the horizontal structure of the electric field also tends to confine the ions beneath the wires. The resulting enhanced ionization will thus give rise to a strong ion flux to the biased wires and the electrode area just below them. Consequently, more secondary electrons will be emitted and will result in the formation of plasma filaments beneath each wire. The enhanced plasma density away from the grid can be explained by the suppressed/reduced diffusion of the electrons/ions across the magnetic field and the slightly lower plasma potential with respect to the case with no bias which changes the loss/gain balance of the electrons and the ions.

The fifth simulation was run for $B = 0.5$ T and $V_g = +60$ V. It can be seen in figure 13(e), the magnetic field has again a strong effect on every plasma parameter. However, the effects on the plasma parameters are inverted. The ion and electron densities are now strongly increased between the wires while the plasma density just beneath the wires is reduced. The plasma potential is still strongly influenced by the presence of the biased wires and the structures propagate vertically down to the sheath above the powered electrode. However, note that the plasma potential beneath the wire is now higher than in between the wire and far away from the grid. The potential structure is again passed on the $x-$component of the electric field which can be seen just beneath the edge of the wires but with direction reversed with respect to the case at $B = 0.5$ T and $V_g = -60$ V. The main difference with the case at $V_g = -60$ V is that the electrons beneath the wires are now much more likely to be captured by the wires therefore preventing ionization in this region. Since the diffusion across the magnetic field lines is strongly reduced, these regions cannot be refilled and appear as depletion regions. In the gap between the wires, the potential drop in the sheath is much larger allowing the electron to gain more energy and therefore enhancing ionization. The ions in the gap between the wires tend to be confined by the structure of the of the electric field and will therefore diffuse even less efficiently towards the regions away from the wires.

These 2D PIC simulations complement the fluid simulation by taking into account secondary electron emission from the surfaces, the RF excitation, and considering the bias voltage

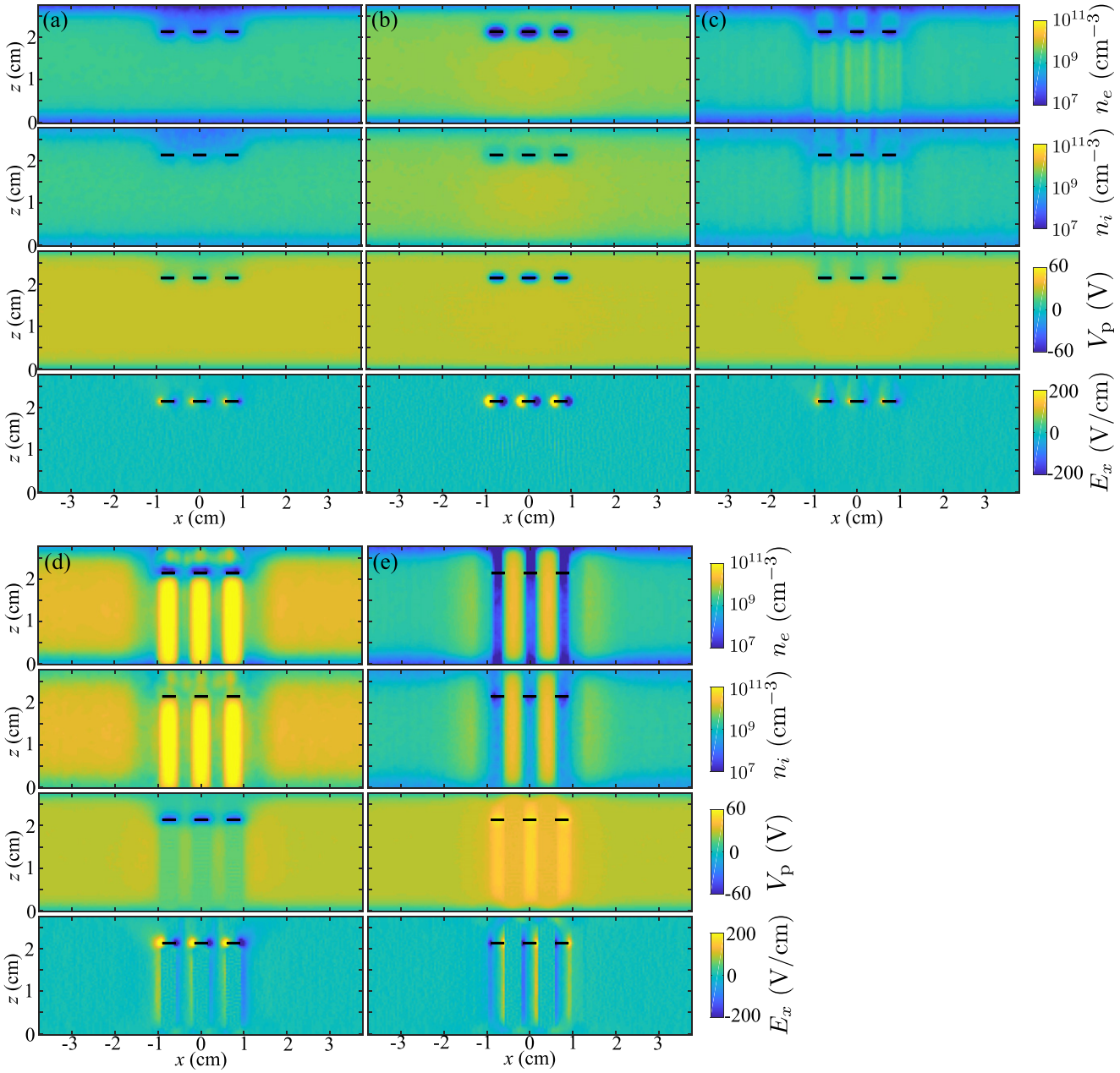

Figure 13. PIC simulation results for different discharge parameters: (a) $B = 0$ mT, $V_g = 0$ V, (b) $B = 0$ T, $V_g = -60$ V, (c) $B = 0.5$ T, $V_g = 0$ V, (d) $B = 0.5$ T, $V_g = -60$ V, (e) $B = 0.5$ T, $V_g = +60$ V. For each subfigures: First line: electron density profiles; second line: ion density profiles; third line: plasma potential profiles; fourth line: profiles of the electric field x–component. Each profile is an average of 5 RF periods after a simulation of 250 RF periods

on the wire mesh. It can be seen in figures 13(c)–(e) that the region directly beneath the edge of the wires is a transition region that connects the quasi-independent plasmas beneath the mesh and in the gap between the mesh wires. Since the plasma potential on the sides of these transition regions are different, there must be a strong electric field with an important x–component. This electric field structure extends along the magnetic field and can be sufficient to trap the dust particles and lead to the appearance of gridding phenomenon below the edges of the wide wire mesh.

4. Conclusion

The effects of placing a wide wire mesh (also called ‘waffle’ electrode) in the bulk of a strongly magnetized plasma were studied experimentally. A new double-head probe was designed and built to perform spatially resolved measurements of the floating potential and electric field beneath the mesh at high magnetic fields. It was observed in the experiments that the presence of the ‘waffle’ electrode imposes a potential profile and electric field in the magnetized plasma that peaks in

the regions beneath the edges of the 'waffle' electrode. Due to this imposed structure, when dust particles were added to the experiment, they mainly became trapped beneath the edges of the 'waffle' electrode. These observations are different from the one observed in the experiments using narrow-wire meshes in which, it seemed that the dust particles were trapped right below the wires of the mesh [65].

Moreover, the effects of placing the metal mesh in magnetized plasmas was investigated numerically using fluid and PIC simulations. These two models complemented each other as $E \times B$ drift and cross-field diffusion of the ions were considered in the fluid model, while secondary electron emission from the surfaces and application of bias voltage on the mesh were modeled in the PIC simulations. It was noticed in both simulations that, at high magnetic fields, the plasma beneath the wires of the mesh is different from the plasma between the wires. This is due to the different, reduced cross-field diffusion of the electrons and ions. A strong electric field could exist in the transition region that connects quasi-independent plasmas beneath the mesh and in the gap between the mesh wires. This electric field structure that is extended parallel to the magnetic axis can explain the trapping of dust particles beneath the edges of the 'waffle' electrode.

In the future studies, the influence of wire width and wire spacing will be systematically investigated, both experimentally and numerically. A special attention will be given to the effects of the Debye length, ions mean-free-path and electron/ion gyro-radii.

Acknowledgments

This work was supported by funds from the National Science Foundation EPSCoR program (OIA-1655280) and US Department of Energy (SC-0016330). L Couëdel acknowledges the support of the Natural Sciences and Engineering Research Council of Canada (NSERC), RGPIN-2019-04333.

ORCID iDs

Mohamad Menati https://orcid.org/0000-0003-1390-137X
Lénaïc Couëdel https://orcid.org/0000-0003-0749-9273

References

[1] Goertz C K 1989 *Rev. Geophys.* **27** 271–92
[2] Hartquist T W, Pilipp W and Havnes O 1996 *Astrophys. Space Sci.* **246** 243–89
[3] Mestel L and Spitzer L Jr 1956 *Mon. Not. R. Astron. Soc.* **116** 503–14
[4] Ivlev A, Röcker T, Vasyunin A and Caselli P 2015 *Astrophys. J.* **805** 59
[5] Horányi M, Morfill G and Grün E 1993 *Nature* **363** 144
[6] Mitchell C J, Horanyi M, Havnes O and Porco C C 2006 *Science* **311** 1587–9
[7] Horányi M, Szalay J, Kempf S, Schmidt J, Grün E, Srama R and Sternovsky Z 2015 *Nature* **522** 324
[8] Horanyi M and Mendis D 1985 *Astrophys. J.* **294** 357–68
[9] Mendis D and Horányi M 2013 *Rev. Geophys.* **51** 53–75
[10] Pelletier J 2000 *Plasma Phys. Controlled Fusion* **42** 227
[11] de Angelis U, Capobianco G, Marmolino C and Castaldo C 2006 *Plasma Phys. Controlled Fusion* **48** B91–7
[12] Winter J 1998 *Plasma Phys. Controlled Fusion* **40** 1201–10
[13] Kobayashi H 2011 *Japan. J. Appl. Phys.* **50** 08JE01
[14] Kortshagen U R, Sankaran R M, Pereira R N, Girshick S L, Wu J J and Aydil E S 2016 *Chem. Rev.* **116** 11061–127
[15] Santos M, Reeves B, Michael P, Tan R, Wise S G and Bilek M M 2019 *Commun. Phys.* **2** 52
[16] Couëdel L *et al* 2019 *Plasma Res. Express* **1** 015012
[17] Thomas Jr E, Merlino R L and Rosenberg M 2012 *Plasma Phys. Controlled Fusion* **54** 124034
[18] Thomas E, Merlino R L and Rosenberg M 2013 *IEEE Trans. Plasma Sci.* **41** 811–5
[19] Merlino R L, Thomas E, Lynch B, LeBlanc S, Hall T, Konopka U and Rosenberg M 2018 *AIP Conf. Proc.* **1928** 020011
[20] Shukla P K and Mamun A A 2002 *Introduction to Dusty Plasma* (Bristol: IOP Publishing)
[21] Nunomura S, Ohno N and Takamura S 1997 *Japan. J. Appl. Phys.* **36** 877–83
[22] Konopka U, Samsonov D, Ivlev A V, Goree J, Steinberg V and Morfill G E 2000 *Phys. Rev.* E **61** 1890–8
[23] Sato N, Uchida G, Kaneko T, Shimizu S and Iizuka S 2001 *Phys. Plasmas* **8** 1786–90
[24] Sato N 2002 *AIP Conf. Proc.* **649** 66–73
[25] Kaw P K, Nishikawa K and Sato N 2002 *Phys. Plasmas* **9** 387–90
[26] Cheung F, Samarian A and James B 2003 *New J. Phys.* **5** 75
[27] Dzlieva E S, Dyachkov L G, Novikov L A, Pavlov S I and Karasev V Y 2018 *Europhys. Lett.* **123** 15001
[28] Dzlieva E S, D'yachkov L G, Novikov L A, Pavlov S I and Karasev V Y 2019 *Plasma Sources Sci. Technol.* **28** 085020
[29] Karasev V Y, Dzlieva E S, Pavlov S I, Novikov A N and Mashek I Ch 2020 *Tech. Phys. Lett.* **46** 371–3
[30] Vasil'ev M, D'yachkov L, Antipov S, Petrov O and Fortov V 2007 *J. Exp. Theor. Phys. Lett.* **86** 358–63
[31] Melzer A, Krüger H, Schütt S and Mulsow M 2019 *Phys. Plasmas* **26** 093702
[32] Kakad A, Lakhina G and Singh S 2003 *Planet. Space Sci.* **51** 177–81
[33] Banerjee D, Janaki M S and Chakrabarti N 2012 *Phys. Rev.* E **85** 066408
[34] Birk G T and Wiechen H 2002 *Phys. Plasmas* **9** 964–70
[35] D'Angelo N 1965 *Phys. Fluid.* **8** 1748–50
[36] Kent G I, Jen N C and Chen F F 1969 *Phys. Fluid.* **12** 2140–51
[37] Tiwari S K, Das A, Angom D, Patel B G and Kaw P 2012 *Phys. Plasmas* **19** 073703
[38] Tsytovich V N, Sato N and Morfill G E 2003 *New J. Phys.* **5** 43
[39] Salimullah M, Sandberg I and Shukla P K 2003 *Phys. Rev.* E **68** 027403
[40] Kalita D, Kakati B, Saikia B K, Bandyopadhyay M and Kausik S S 2015 *Phys. Plasmas* **22** 113704
[41] Jovanović J and Shukla P K 2004 *Phys. Scr.* **T107** 188
[42] Jovanović D and Shukla P 2004 *Phys. Lett.* A **329** 334–40
[43] Tadsen B, Greiner F and Piel A 2014 *Phys. Plasmas* **21** 103704
[44] Konopka U, Schwabe M, Knapek C, Kretschmer M and Morfill G E 2005 *AIP Conf. Proc.* **799** 181–4
[45] Schwabe M, Konopka U, Bandyopadhyay P and Morfill G E 2011 *Phys. Rev. Lett.* **106** 215004
[46] Bandyopadhyay P, Sharma D, Konopka U and Morfill G 2014 *AIP Conf. Proc.* **1582** 281–7
[47] Thomas E, Konopka U, Merlino R L and Rosenberg M 2016 *Phys. Plasmas* **23** 055701
[48] Menati M, Thomas E and Kushner M J 2019 *Phys. Plasmas* **26** 063515
[49] Thomas E, Lynch B, Konopka U, Merlino R L and Rosenberg M 2015 *Phys. Plasmas* **22** 030701

[50] Thomas E, Konopka U, Lynch B, Adams S, LeBlanc S, Merlino R L and Rosenberg M 2015 *Phys. Plasmas* **22** 113708
[51] Hall T, Thomas E, Avinash K, Merlino R and Rosenberg M 2018 *Phys. Plasmas* **25** 103702
[52] Jaiswal S, Menati M, Couëdel L, Holloman V H, Rangari V and Thomas E 2020 *Japan. J. Appl. Phys.* **59** SHHC07
[53] Thomas E Jr 2017 *J. Plasma Fusion Res.* **93** 1
[54] Menati M, Rasoolian B, Thomas E and Konopka U 2020 *Phys. Plasmas* **27** 022101
[55] Thomas E, Konopka U, Artis D, Lynch B, Leblanc S, Adams S, Merlino R L and Rosenberg M 2015 *J. Plasma Phys.* **81** 345810206
[56] Tomita Y, Smirnov R and Zhu S 2005 *Plasma Sci. Technol.* **7** 2657–9
[57] Niknam A R, Haghtalab T and Khorashadizadeh S M 2011 *Phys. Plasmas* **18** 113707
[58] González J and Conde L 2019 *Phys. Plasmas* **26** 043505
[59] Graves D B and Jensen K F 1986 *IEEE Trans. Plasma Sci.* **14** 78–91
[60] Wilcoxson M H and Manousiouthakis V I 1993 *IEEE Trans. Plasma Sci.* **21** 213–22
[61] Akashi H, Sakai Y, Takahashi N and Sasaki T 1999 *J. Phys. D: Appl. Phys.* **32** 2861–70
[62] Derzsi A, Hartmann P, Korolov I, Karácsony J, Bánó G and Donkó Z 2009 *J. Phys. D: Appl. Phys.* **42** 225204
[63] Liu Q, Liu Y, Samir T and Ma Z 2014 *Phys. Plasmas* **21** 083511
[64] Eliseev S I, Bogdanov E A and Kudryavtsev A A 2017 *Phys. Plasmas* **24** 093503
[65] Hall T 2019 *PhD Thesis* Auburn University
[66] Chen F 2015 *Introduction to Plasma Physics and Controlled Fusion* (Berlin: Springer)
[67] Belenguer P and Boeuf J P 1990 *Phys. Rev.* A **41** 4447–59
[68] Bojarov A, Radmilović-Radjenović M and Petrović Z L 2010 *Publ. Astron. Obs. Belgrade* **89** 131–4
[69] Nieter C and Cary J R 2004 *J. Comput. Phys.* **196** 448–73
[70] Phelps A V and Petrovic Z L 1999 *Plasma Sources Sci. Technol.* **8** R21–44